The role of shallow convection in the momentum budget of the trades from large-eddy-simulation hindcasts

Helfer, Kevin C.; Nuijens, Louise; Vijay Dixit, V.

DOI
10.1002/qj.4035

Publication date
2021

Document Version
Final published version

Published in
Quarterly Journal of the Royal Meteorological Society

Citation (APA)
Helfer, K. C., Nuijens, L., & Vijay Dixit, V. (2021). The role of shallow convection in the momentum budget of the trades from large-eddy-simulation hindcasts. *Quarterly Journal of the Royal Meteorological Society*, *147*(737), 2490-2505. https://doi.org/10.1002/qj.4035

Received: 11 September 2020 | Revised: 15 March 2021 | Accepted: 26 March 2021 | Published on: 20 April 2021

DOI: 10.1002/qj.4035

Quarterly Journal of the Royal Meteorological Society RMetS

RESEARCH ARTICLE

The role of shallow convection in the momentum budget of the trades from large-eddy-simulation hindcasts

Kevin C. Helfer | **Louise Nuijens** | **Vishal V. Dixit**

Department of Geoscience and Remote Sensing, Delft University of Technology, Delft, Netherlands

Correspondence
K. C. Helfer, Delft University of Technology, Stevinweg 1, 2628CN Delft, The Netherlands.
Email: k.c.helfer@tudelft.nl

Funding information
European Union's Horizon 2020 research and innovation programme, Grant/Award Number: 714918

Abstract

Motivated by the abundance of low clouds in the subtropics, where the easterly trade winds prevail, we study the role of shallow convection in the momentum budget of the trades. To this end, we use ICON-LEM hindcasts run over the North Atlantic for 12 days corresponding to the NARVAL1 (winter) and NARVAL2 (summer) flight campaigns. The simulation protocol consists of several nested domains, and we focus on the inner domains ($\approx 100 \times 100\,\mathrm{km}^2$) which have been run at resolutions of 150–600 m and are forced by analysis data, thus exhibiting realistic conditions. Combined, the resolved advection and the subgrid stresses decelerate the easterly flow over a frictional layer that balances the prevailing geostrophic wind forcing. Irrespective of the horizontal resolution, this layer is about 2 km deep in the strong winter trades and 1 km in summer, as winds and geostrophic forcing weaken and cloudiness reduces. The unresolved processes are strongest near the surface and are well captured by traditional K-diffusion theory, but convective-scale motions which are not considered in K-diffusion theory contribute the most in the upper part of the mixed layer and are strongest just below cloud base. The results point out that convection in the mixed layer – the roots of trade-wind cumuli and subcloud-layer circulations – play an important role in slowing down easterly flow below cloud base (but little in the cloud layer itself), which helps make the zonal wind jet more distinct. Most of the friction within the clouds and near the wind jet stems from smaller-scale turbulence stresses.

KEYWORDS

convective momentum transport, K-diffusion, large-eddy simulation, momentum budget, shallow convection, trade winds

1 | INTRODUCTION

The trade winds are easterly winds that prevail over the tropical and subtropical oceans north and south of the Equator. They form the inflow branches of the large-scale Hadley circulation and influence patterns of convergence and tropical rainfall. Furthermore, they modulate turbulent heat fluxes and stresses at the sea surface, and through these sea-surface temperatures and ocean mixing. Therefore, it is important to understand the structure of the trade winds and the processes that influence this structure. One of those processes is shallow convection, which leads to ubiquitous cumulus clouds across the trades and has long been known to play an important role in setting boundary-layer temperature and humidity (Riehl *et al.*, 1951; Malkus, 1958; Tiedtke *et al.*, 1988; Neggers *et al.*, 2007). However, its role in the horizontal momentum budget, such as whether it contributes to mixing slow near-surface momentum upwards (and hence acts as a frictional force), is not well understood.

Earlier works investigating the vertical wind structure in the trades include studies by Riehl *et al.* (1951) using WWII weather ship data collected in the North Pacific as well as the momentum budget reconstructions using radiosonde arrays from the Barbados Oceanographic and Meteorological Experiment (BOMEX; Holland and Rasmusson, 1973) and the Atlantic Tradewind Experiment (ATEX; Augstein *et al.*, 1974; Brümmer *et al.*, 1974). In these studies, the frictional force arising from Reynolds stresses is derived as a residual from other terms in the momentum budget, for example the large-scale advection, pressure-gradient and Coriolis forces. In their reconstruction of the momentum budget during ATEX, Brümmer *et al.* (1974) in particular pointed out that turbulent stresses do not vanish at the mixed-layer top or base of the cloud layer. They hypothesized that an additional source of stress could stem from convection, which would help explain discrepancies between derived and measured surface-drag coefficients.

A similar point has been made by studies that explain patterns of surface winds over tropical oceans. Traditionally, tropical surface winds have been explained using Rayleigh damping models that take the generalised Ekman balance as a starting point (e.g., Deser, 1993). These models assume a balance between pressure gradients, Coriolis acceleration and friction:

$$f\mathbf{k}\times\overline{\mathbf{u}}+\frac{1}{\rho_0}\nabla\overline{p}=\frac{\partial\boldsymbol{\tau}}{\partial z}, \tag{1}$$

where the overbar $\bar{\cdot}$ indicates slab averages, f is the Coriolis parameter, $\mathbf{u}$ is the wind vector, ρ_0 is a reference density (that depends on the specific model implementation), p is the pressure and $\boldsymbol{\tau}$ is the stress tensor. These models neglect viscosity and model the friction as a linear function of the surface wind speed ($\partial_z\boldsymbol{\tau} = -\eta\mathbf{U}$) which goes to zero at the top of the boundary layer, which in the Tropics is typically taken as the subcloud layer. This implies that there is no vertical mixing of momentum at the boundary-layer top that can play a role in setting surface- (and boundary-)layer winds. However, using a mixed-layer model that includes a bulk parametrization for entrainment at the top of the boundary layer to estimate boundary-layer winds, Stevens *et al.* (2002) and Back and Bretherton (2009) demonstrate that the acceleration of near-surface winds by mixing momentum between the boundary layer and the free troposphere is key to explaining the climatology of surface winds in the Tropics. The mixed-layer model does not explicitly take into account convective momentum transport (CMT), but a convective mass flux is implicit in the formulation of an entrainment or exchange flux at the mixed-layer (boundary-layer) top. In another study, Carr and Bretherton (2001) derived CMT as a residual from the large-scale budget of momentum using reanalysis data and found CMT to be larger in the lower troposphere than in the upper troposphere, suggesting that the abundance of shallow convection could lead to a source of shallow CMT which would be important for large-scale circulations. Similarly, Lin *et al.* (2008) stated that CMT is a factor that damps the low-level trade wind. Using general circulation model (GCM) simulations, Richter *et al.* (2014) suggested that CMT is crucial for explaining the strength and direction of surface winds over the equatorial Atlantic.

In none of these studies, the relative influence of small-scale turbulence versus more coherent thermal plumes associated with convection on the total momentum transport within the boundary layer is specifically analysed. This is the objective of our study, in which we ask: What is the role of shallow convection in the momentum budget of the trades? In our answer, we aim to differentiate between different scales of motion from turbulent to overturning motions. We also address whether moist convection contributes meaningfully to turbulent stresses at the mixed-layer top (approximately cloud base) and whether the profile of the momentum flux within the well-mixed subcloud layer behaves according to the established K-diffusion model. This parametrization models the momentum flux $\boldsymbol{\tau}$ as the product of the mean wind shear $\partial_z\overline{\mathbf{u}}$ and a height-dependent exchange coefficient K, thus assuming that turbulent momentum mixing is isotropic in the horizontal but dependent on the mixing length-scale in the vertical (e.g., Holtslag and Boville, 1993; Stevens, 2000). Such K-diffusion models can be extended by a non-local term or even be combined with a mass-flux approach to account for counter-gradient transport and mixing at longer length-scales (Soares *et al.*, 2004; Siebesma *et al.*, 2007).

We make use of a unique set of high-resolution simulations run with the ICON large-eddy model in hindcast mode over a domain spanning the entire North Atlantic trades (Stevens *et al.*, 2019). Unlike conventional large-eddy-simulation (LES) cases, these hindcasts are initialized and forced with ECMWF analysis data at the outer domain boundaries, so that smaller inner domains on the order of a few 100×100 km^2 feel a realistically varying large-scale state with air masses moving in at one boundary and moving out at the other – as opposed to the traditionally used periodic boundary conditions. The dataset covers twelve days in both summer and winter with a variety of atmospheric states and cloud regimes, including days with shallow and deeper convection. The inner domains have been run with different resolutions, which allows us to infer the importance of eddies of different scales. The dataset has already offered a wealth of new insights, for example on the diurnal cycle of marine shallow convection (Vial *et al.*, 2019), the shallow-convective mass flux (Vogel *et al.*, 2020), the vertical distribution of lower-tropospheric water vapour (Naumann and Kiemle, 2020) and counter-gradient momentum transport (which we also briefly discuss below; Dixit *et al.*, 2021).

This paper is structured as follows. We first describe the ICON-LEM simulations and our analysis of the momentum budget (Section 2). In Section 3, we analyse the momentum budget for winter and summer days and look closer at the role of shallow convection versus small-scale turbulence in setting the frictional force, in particular. Section 4 discusses the momentum flux and, in particular, how it relates to the K-diffusion model. Finally, we summarise our findings in Section 5.

2 | DATA DESCRIPTION

We analysed LES hindcasts which were performed on specific days of the Next-Generation Advanced Remote Sensing for Validation (NARVAL) expeditions (Stevens *et al.*, 2019), using the Icosahedral Non-hydrostatic (ICON) model (Zängl *et al.*, 2015) as an LES (ICON-LEM; Dipankar *et al.*, 2015). These simulations cover an extensive part of the tropical North Atlantic (Figure 1). Six days in December 2013 and six days in August 2016 have been simulated (Table 1). The simulation protocol consisted of five nested domains which decrease both in size and in horizontal grid spacing from 2,500 m to 150 m (Figure 1); the domains were coupled via a one-way nesting. The vertical grid was the same in all domains, and its spacing was stretched from about 30 m at the lowest level to about 300 m at 20 km, implying that in the lower troposphere vertical transport is well resolved. Here, we only consider the three smallest domains, which used LES physics, while the two largest domains used NWP physics (discussed by Klocke *et al.*, 2017). The LES runs had horizontal resolutions of 600, 300 and 150 m. While even 150 m is probably on the coarser end of what is needed to simulate shallow cumuli (e.g., Sato *et al.*, 2018), comparison with satellite imagery shows that the simulations are able to capture many important features of the cloud field (Vial *et al.*, 2019). Besides, one should also value the great size of the simulation domain and the realistic forcing. The runs were initialised at 0900 UTC each day, using data from the larger domains, which in turn were initialised using ECMWF analysis data and forced at the outermost boundaries using 3-hourly ECMWF forecasts. The model was then run for 27 hr, whereby the first 3 hr were disregarded as model spin-up. We emphasise that the modelling approach here is unlike typical idealised LES studies. In particular, there were no periodic boundary conditions, subsidence was not prescribed and the runs were not initialised with laterally homogeneous profiles. Further details can be found in Stevens *et al.* (2019).

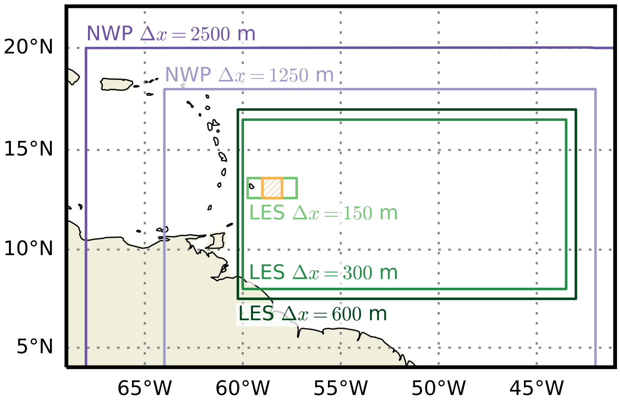

FIGURE 1 Overview of the simulation protocol of Stevens *et al.*, (2019) with two outer domains which use NWP physics (purple) and three inner domains which use LES physics (green). The domains are coupled via a one-way nesting, and the horizontal resolution Δx increases as the domain size decreases. The hatched orange square indicates the area of interest of the present paper [Colour figure can be viewed at wileyonlinelibrary.com]

Here, we consider a subset of the smallest simulation domain with an area of $1° \times 1°$ ($\approx 100 \times 100$ km^2), which is similar to a typical GCM grid box. The box is located east of Barbados (58–59°W, 12.6–13.6°N; orange square in Figure 1) and coincides with the main operational area of the EUREC^{4}A (ElUcidating the RolE of Clouds–Circulation Coupling in Climate), a field campaign which took place in early 2020 (Stevens *et al.*, 2021).

Within that area, we calculated *a posteriori* all contributions to the horizontal momentum equation

TABLE 1 Overview of the simulated days

Campaign	Research flight	Date
NARVAL1	RF 2	11 December 2013
	RF 3	12 December 2013
	RF 4	14 December 2013
	RF 5	15 December 2013
	RF 6	16 December 2013
	RF 8	20 December 2013
NARVAL2	RF 2	10 August 2016
	RF 3	12 August 2016
	RF 5	17 August 2016
	RF 6	19 August 2016
	RF 7	22 August 2016
	RF 8	24 August 2016

at every grid point of the LES output, which is available every 15 min. The LES solves the filtered Boussinesq-approximated momentum equation, which for the horizontal wind components reads (e.g., Stull, 1988):

$$\frac{\partial \widetilde{u}_i}{\partial t} = \underbrace{f\varepsilon_{ij3}\widetilde{u}_j}_{C} \underbrace{-\frac{1}{\rho}\frac{\partial p}{\partial x_i}}_{P} \underbrace{-\widetilde{u}_j\frac{\partial \widetilde{u}_i}{\partial x_j}}_{A} \underbrace{-\frac{\partial \tau_{ij}}{\partial x_j}}_{R}, \tag{2}$$

where the tildes $\widetilde{\cdot}$ indicate the LES-filtered variables, u_i are the horizontal wind components in the x- and y-direction ($i = 1, 2$), f is the Coriolis parameter, ε_{ij3} is the Levi-Civita symbol, ρ is the density, p is the pressure and τ_{ij} is the subgrid stress tensor. (In the following, we drop the tildes for convenience.) The first term on the right-hand side of the equation depicts the Coriolis effect (C), the second the pressure-gradient force (P) and the third the resolved advection (A), which may be decomposed into horizontal and vertical components:

$$\underbrace{-u_j\frac{\partial u_i}{\partial x_j}}_{A} = \underbrace{-u\frac{\partial u_i}{\partial x} - v\frac{\partial u_i}{\partial y}}_{A_\mathrm{h}} \underbrace{-w\frac{\partial u_i}{\partial z}}_{A_\mathrm{v}}. \tag{3}$$

The fifth term of Equation (2) corresponds to stresses introduced on scales smaller than the LES model grid: the subgrid turbulence, calculated using a Smagorinsky turbulence scheme. This term is calculated as a residual R, while output of the subgrid tendencies or fluxes (apart from the surface fluxes) are not available. Note that this approach implies that R may also contain any other errors that may occur in the analysis (e.g., from the re-gridding mentioned below). Furthermore, we remark that, due to ICON's triangular grid, the exact form of the Navier–Stokes equation solved by the model is slightly different, though the principles discussed before still hold (Dipankar *et al.*, 2015).

To calculate the budget terms, the model output was first re-gridded from the model's unstructured grid to a Cartesian grid of similar resolution. Derivatives were computed using second-order central differences. The storage term on the left-hand side of the equation was calculated as the temporal derivative of the outputted wind field. We then spatially averaged each term of Equation (2) on each model level over the whole 1° × 1° area. These spatial averages were consecutively averaged over six 2-hr periods (1200–1400 UTC, 1600–1800 UTC, and so on, until 0800–1000 UTC of the following day) of each of the twelve simulation days. This gave us a reliable statistical basis for our analysis of the mean momentum budget, while keeping the computational demand in check. Furthermore, by analysing the budget throughout the day, we were mindful of the diurnal cycle which is present even over the ocean (Vial *et al.*, 2019). Mesoscale variability, which can introduce large hourly variations, is beyond the scope of this study.

3 | THE MOMENTUM BUDGET

3.1 | Mean state of winter and summer NARVAL days

The area upstream of Barbados is governed by two distinct seasons: a wet season from about June until November and a dry season throughout the rest of the year (Brueck *et al.*, 2015). These seasons are tied to the location of the intertropical convergence zone (ITCZ). In the dry season, the ITCZ is located at lower latitudes, and the area east of Barbados experiences steady trade winds from east to northeast, moderate large-scale subsidence and an inversion at around 800 hPa visible in profiles of both temperature and relative humidity. In contrast to this, in the wet season, the ITCZ is located much closer to Barbados, leading to weaker winds from the east (at times even southeast), moderate upward motion and a less-defined trade inversion.

Figure 2 showcases these differences between August (red lines) and December days (blue lines): typical trade-wind conditions with shallow convection in boreal winter and deeper convection in boreal summer. The figure shows 2-hr averages as thin lines and the mean over all winter days as thick blue lines and all summer days as thick red lines. In December, we have a trade-wind layer

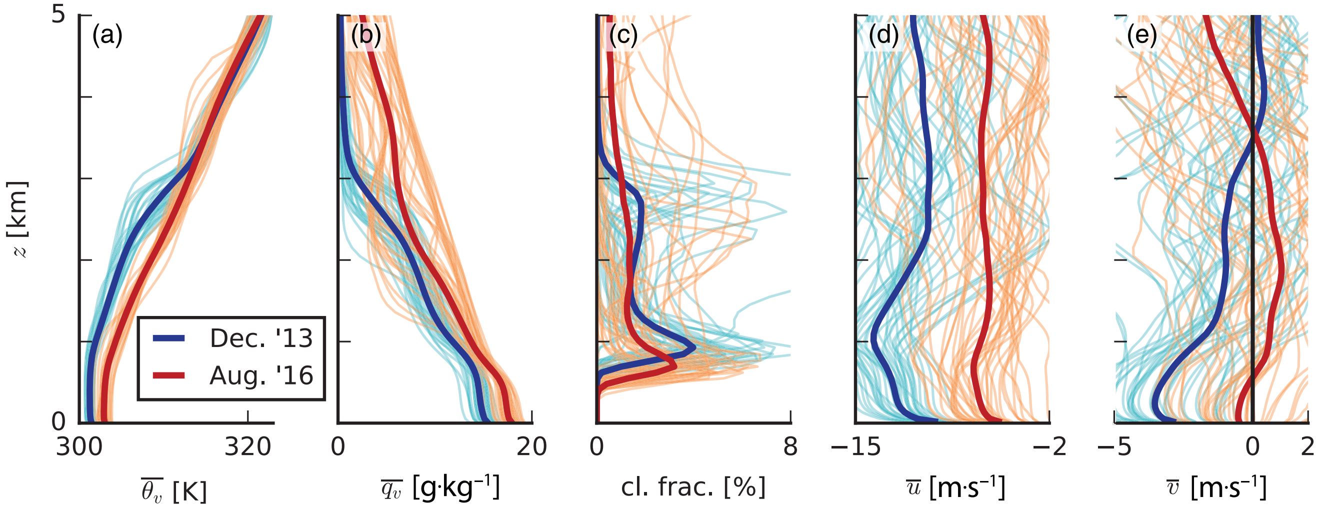

FIGURE 2 Slab-averaged profiles of (a) virtual potential temperature θ_v, (b) water vapour specific humidity q_v, (c) cloud fraction, (d) zonal wind speed u and (e) meridional wind speed v. The thin lines indicate 2-hr averages and the thick lines indicate averages over all simulated days in December (blue) and August (red) [Colour figure can be viewed at wileyonlinelibrary.com]

with a clear inversion, trade winds from eastnortheast at the surface and a cloud fraction profile that always has a maximum just above cloud base and frequently also near the inversion. Such a cloud fraction profile is typical for the winter trades near Barbados where shallow cumuli are often accompanied by a stratiform cloud layer near the trade-wind inversion (Nuijens *et al.*, 2014). On average, the December cloud fraction maximum in our simulations is around 4%, which is also in line with the observations of Nuijens *et al.* (2014). In August, the boundary layer is somewhat warmer and moister without an inversion, surface winds are much weaker and from the east, and the cloud fraction profile often has one maximum only near cloud base as well as higher cloud tops.

The typical wind profile in the North Atlantic trades is dominated by the zonal component and is characterised by steady easterlies to northeasterlies near the surface, a wind speed maximum near cloud base and decreasing wind speed further aloft (e.g., Holland and Rasmusson, 1973; Brümmer *et al.*, 1974; Brueck *et al.*, 2015). Figure 2c shows that we find most of these features on the simulated days. In particular, the dominance of the zonal component and the wind speed maximum near cloud base are well captured during winter. An important difference between the wind as calculated from the simulation output and for example the BOMEX wind profiles is the wind above 2.5 km. While in BOMEX the zonal wind speed continues to decrease with height, that is, become less negative (Holland and Rasmusson, 1973), the mean zonal wind during NARVAL is approximately constant with height. Such a near-constant wind with height is not typical on individual days, but reflects the large high day-to-day variability in wind shear at those levels.

We define the wind turning angle as the difference between the actual wind direction and the geostrophic wind direction and show it in Figure 3 together with the total wind speed and the wind direction. In winter, the wind turning angle is negative near the surface and decreases to zero throughout a layer of about 1.5 km deep. The negative angle indicates that the actual wind comes from the northeast, rather than from the east, which implies that the wind has turned across isobars towards lower pressure at the Equator, as identified in earlier studies of (sub)tropical winds (Brümmer *et al.*, 1974; Stevens *et al.*, 2002). In summer, there is much more variability in the wind turning and an ageostrophic wind component is more common even at higher altitudes. This would be in line with slow momentum from near the surface being transported across a deeper layer in summer due to deeper convection, introducing a so-called Şcumulus frictionŤ. In the next sections, we look closer at the different processes in the momentum budget to identify the role of convection.

3.2 | Momentum tendencies

First considering the simulations at the highest horizontal resolution of 150 m, the different momentum tendencies as defined in Equation (2) are shown in Figure 4 with the means for winter and summer separately. Figure 4a–e show the zonal component and Figure 4f–j the meridional component. All tendencies except for the residual show significant variability in both sign and magnitude in the two-hourly profiles (thin lines in Figure 4). However, on average, the storage term is negligible at all heights. The pressure gradient dominates in the north–south direction

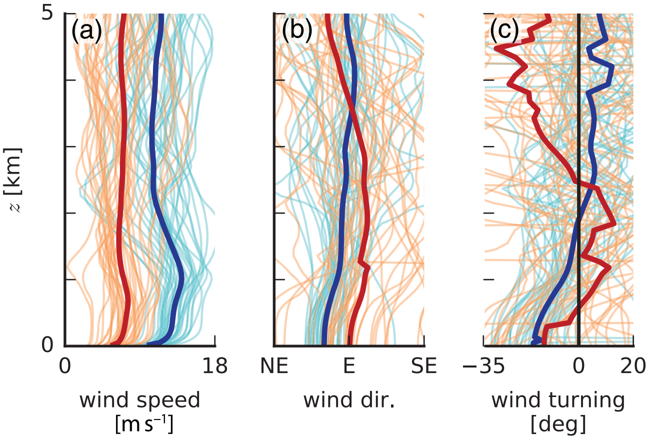

FIGURE 3 Slab-averaged profiles of (a) total wind speed, (b) wind direction and (c) wind turning (with respect to purely geostrophic flow). A negative wind turning angle here means more northerly wind and a positive angle more southerly wind. The line styles and colours are the same as in Figure 2 [Colour figure can be viewed at wileyonlinelibrary.com]

(Figure 4h) and is largely balanced by the Coriolis force (Figure 4g), which leads to the development of predominantly zonal flow. All forces are much weaker in summer than in winter, caused by the weaker pressure-gradient force (Figure 4h, in red) due to the northward wander of the ITCZ.

The resolved advective tendency and the residual tendency (Figure 4d,e,i,j) exhibit large values in the lower 2 km of the atmosphere, whereas above 2 km they are on average negligible. The advective tendency includes all motions on scales equal to and larger than the model grid, whereas the residual tendency is interpreted as subgrid turbulence not resolved by the model grid. These two mostly act in the opposite direction. For instance, the advective tendency is negative close to the surface in both wind components, which indicates an acceleration in the direction of the mean northeasterly wind, whereas the residual tendency is positive, which indicates a deceleration in the direction of the mean wind.

Perhaps the vectors in Figure 5 offer a more intuitive view of these results. The top row shows the direction of the wind, the pressure gradient and Coriolis force, as well as the forcing from the advection and residual tendencies combined, using a vector representation for winter (blue) and summer (red). The vectors are shown at different altitudes: (a) in the surface layer, (b) well into the mixed layer, (c) near cloud base and (d) at the zonal wind jet in the cloud layer. This vector view shows more clearly that the combined vector $A+R$ is not simply opposing the mean surface wind. This implies that it is not merely surface friction that is at play here, but instead mixing across the boundary layer may introduce air masses whose wind is closer to geostrophy, thereby reducing the turning across isobars (Brümmer *et al.*, 1974; Stevens *et al.*, 2002). The bottom row separates the advective from the residual tendencies, and shows that near the surface, the subgrid turbulence (R) is as expected directed almost opposite to the mean wind, whereas the resolved flow (A) is aligned with the mean wind. In the mixed layer (400 m), A is instead directed against the mean wind, and maximizes near cloud base (Figure 4d,i). In other words, resolved advection here tends to reduce the easterly wind component. In the lower cloud layer, near the zonal wind jet (∼1 km), the advective tendency is closer to zero, only to become slightly positive in the cloud layer between 1 and 2 km (Figure 4d,i). In the lower cloud layer, the subgrid turbulence R is again larger with positive values, but only in winter, presumably because the zonal wind jet and thus shear is more pronounced (Figures 4e,j and 5c,d). Combined, $A+R$ have a considerable magnitude at cloud base, which is at least a third of $A+R$ present near the surface.

The advective tendency includes contributions from resolved horizontal and vertical advection (Equation (3)). In Figure 6a,b,g,h, the horizontal and vertical components A_h and A_v of the total advection are shown. The structure of the total advective tendency (Figure 4e) is similar to that of A_h, which acts to accelerate the flow near the surface and slow down the flow in the mixed layer and near cloud base (Figure 6a,g). Vertical advection A_v partially balances these tendencies (Figure 6b,h).

We may ask what the contribution of large-scale wind gradients (both horizontal and vertical) acting on the mean wind is. In the absence of an estimate of the large-scale horizontal wind gradient, we may estimate the contribution from ‘large scales’ by applying a horizontal low-pass filter with a cut-off scale of 10 km to the wind data and then calculating the horizontal advective tendency $A_\mathrm{ls,h}$ (which is plotted in Figure 6c,i) from this ‘smoothed’ wind field. Using a Reynolds decomposition of the wind into a mean and a fluctuating part ($u_i=\overline{u_i}+u_i'$), the large-scale zonal advection (e.g., averaged over our area of interest) may be written as:

$$\overline{u\frac{\partial u}{\partial x}+v\frac{\partial u}{\partial y}+w\frac{\partial u}{\partial z}} \approx \overline{u}\frac{\partial \overline{u}}{\partial x}+\overline{v}\frac{\partial \overline{u}}{\partial y} + \overline{w}\frac{\partial \overline{u}}{\partial z}+\overline{u'\frac{\partial u'}{\partial x}}+\overline{v'\frac{\partial u'}{\partial y}}+\overline{w'\frac{\partial u'}{\partial z}}. \tag{4}$$

We dropped all cross terms (e.g., $\overline{\overline{u}\partial_x u'}+\overline{u'\partial_x \overline{u}}$), in accordance with Reynolds averaging rules. The first three terms on the right-hand side represent larger-scale advection and the last three terms smaller-scale advection on scales smaller than 10 km. The large-scale vertical

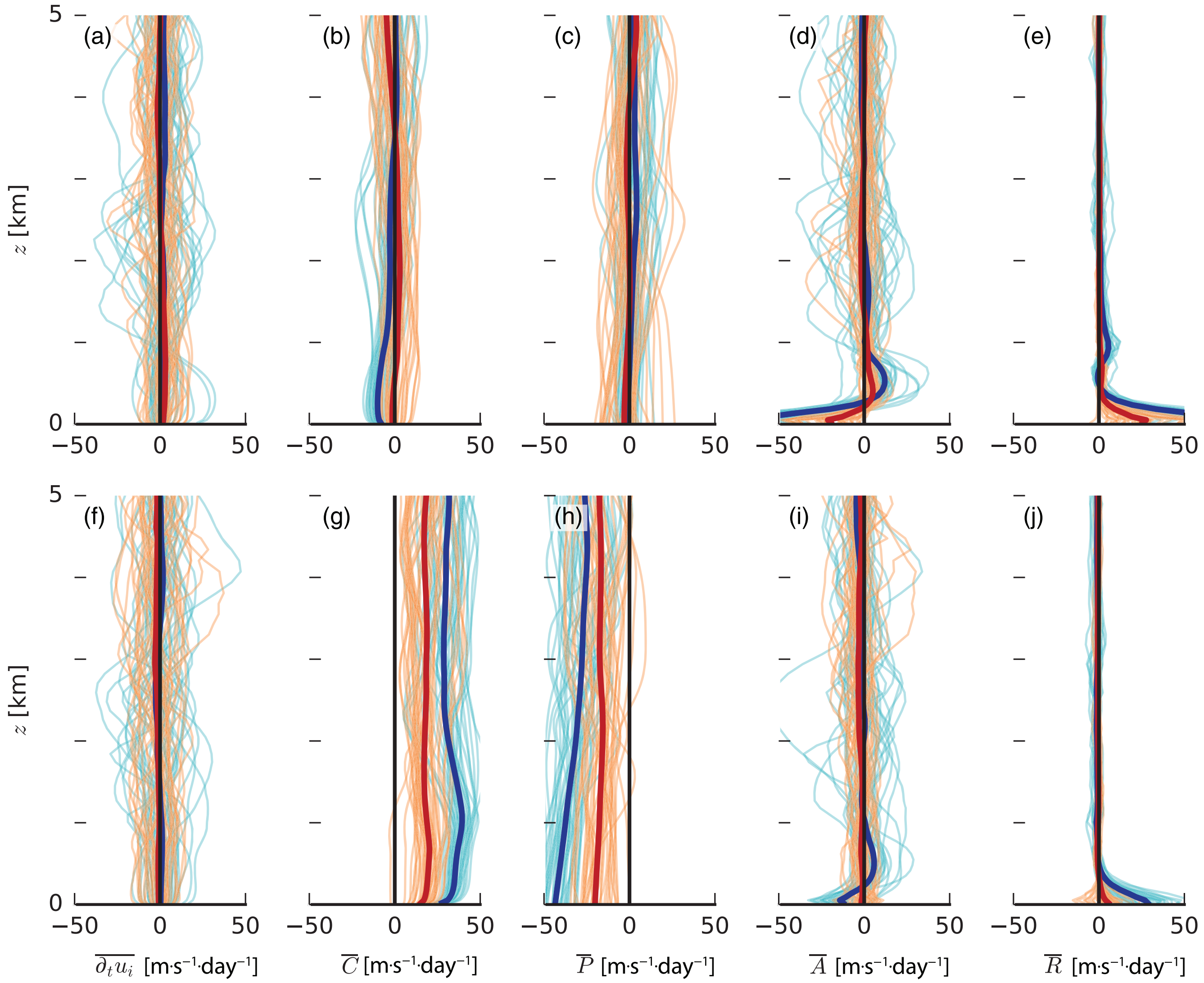

FIGURE 4 Slab-averaged profiles of the terms of the momentum budget (cf. Equation 2) for (a–e) the zonal wind component and (f–j) the meridional component. (a, f) show total tendency $\partial_t u_i$, (b, g) the Coriolis force C, (c, h) the pressure-gradient force P, (d, i) the resolved advection A and (e, j) the residual R. The line styles and colours are the same as in Figure 2 [Colour figure can be viewed at wileyonlinelibrary.com]

advection may be estimated from the product of the domain-mean vertical velocity and the vertical gradient of horizontal wind, which is shown in Figure 6d,j. Neither of the large-scale terms (first three on the right-hand side of Equation (4)) have a systematic structure and sign in the lower atmosphere, with large hour-to-hour variations, which on average are close to zero. This implies that horizontal wind fluctuations ($\overline{u'\partial_x u'} + \overline{v'\partial_y u'} + \overline{w'\partial_z u'}$) on scales smaller than 10 km (i.e., convection and turbulence rather than large-scale circulations) dominate the advective tendencies. Note that the choice of 10 km is somewhat arbitrary, and though we have investigated different values as well (not shown), a longer length-scale seems hardly justified, given that even advection from scales larger than 10 km is negligible.

As in Figure 5, we may combine the advection and residual into one term ($A + R$; Figure 6d,i) and the same for the pressure-gradient and Coriolis forces ($P + C$; Figure 6e,j). The two terms mirror nicely, which reflects the overall balanced budget (Figure 4a,f). This also more clearly reveals the depth of the frictional layer, which we interpret as the layer where the dominant easterlies are decelerated, which extends up to about 2 km in winter and 1 km during summer. Thinking about the concept of cumulus friction (Schneider and Lindzen, 1976) in studies of deep convection, it appears that there is a friction between 1 and 2 km that is about a third of the value in the well-mixed subcloud layer. This is not surprising because of the strong turbulence associated with the clouds at these altitudes.

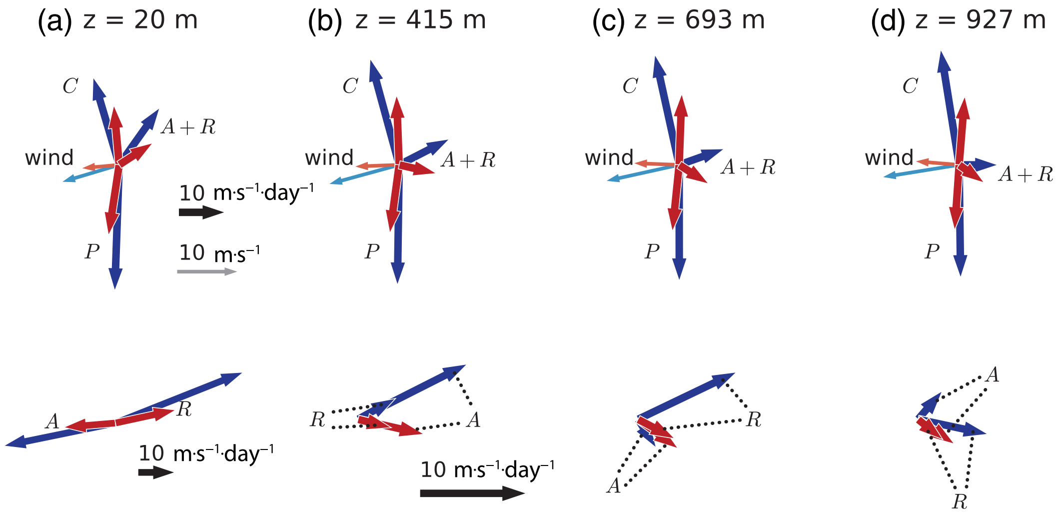

FIGURE 5 Vector representation of the momentum budget averaged over (blue) all December days and (red) all August days (a) near the surface (∼20 m), (b) in the mixed layer (∼400 m), (c) near cloud base (∼700 m) and in the cloud layer (∼900 m). The thinner arrows indicate the wind speed and direction at each height level. The length of the arrows indicates the magnitude of the overall average of the respective budget term or the wind speed (thick lines in Figs. 3 and 4). The scale is the same for the whole top row but different for the panels in the bottom row, as indicated by the black and grey arrows [Colour figure can be viewed at wileyonlinelibrary.com]

3.3 | Resolved momentum fluxes

Further manipulation of the Reynolds-decomposed advection term (Equation 4) shows that the divergence of the momentum flux represents the influence of turbulent stress on the mean motion (e.g., Stull, 1988):

$$\overline{u_j \frac{\partial u_i}{\partial x_j}} \approx \overline{u_j} \frac{\partial \overline{u_i}}{\partial x_j} + \frac{\partial \overline{u_i' w'}}{\partial z}. \tag{5}$$

Note that, while in the previous section (Equation (4)) the primes indicated deviations at scales smaller than 10 km, here they more traditionally indicate deviations from slab averages over the entire 1° × 1° area. To arrive here, the continuity equation multiplied by u_i' was added to Equation (4) and the horizontal momentum flux divergences (e.g., $\partial_x \overline{u'u'} + \partial_y \overline{u'v'}$) were dropped because, according to Gauss's theorem, they are equivalent to the difference between the lateral fluxes at the boundaries, which are found to be small.

We find that the profile of the total advective tendency (Figure 4d,i) is close to that of the vertical divergence of the resolved momentum flux (Figure 7b,f). Given that the large-scale advective tendency (first term on the right-hand side of Equation (5)) is mostly negligible (Figure 6c,d,i,j), this confirms that the horizontal divergence of horizontal momentum flux, which was omitted (and which represents small-scale horizontal advection), indeed plays no important role (Equation (5)). We may thus interpret the resolved momentum fluxes as the main contributors to what we call CMT, including dry and moist convection on scales of 150 m and larger.

As we show in Figure 7, the magnitude of the momentum fluxes is largely determined by the magnitude and structure of the zonal and meridional (geostrophic) wind. The figures shows the daily-averaged profiles of resolved momentum fluxes in the zonal (a–d) and meridional (e–h) directions, along with their negative vertical divergence $-\partial_z \overline{u_i' w'}$. On the horizontal axis of Figure 7a,e, the coloured tick marks correspond to the total turbulent momentum flux at the surface, which reveals the contribution of unresolved fluxes, which is generally largest near the surface. The profiles are coloured by the strength of the respective zonal and meridional surface wind speed, for winter (blue) and summer (red). Stronger surface wind speeds during winter are accompanied by larger shear in the surface and subcloud layers and larger turbulent fluxes. Above approximately 2 km the fluxes are small, even if clouds are still present at those heights (Figure 7c). Deep convection on some of the summer days does not lead to more momentum flux at greater heights. The meridional momentum flux (Figure 7e) is persistently negative from cloud base upwards, suggesting that faster (more negative) momentum from the near-surface meridional jet (Figure 7h) is transported through the clouds. On two summer days with positive surface v and without a near-surface jet, the meridional momentum flux is negative even at the surface.

Near the surface, the resolved zonal flux divergence is negative, which is associated with an acceleration of

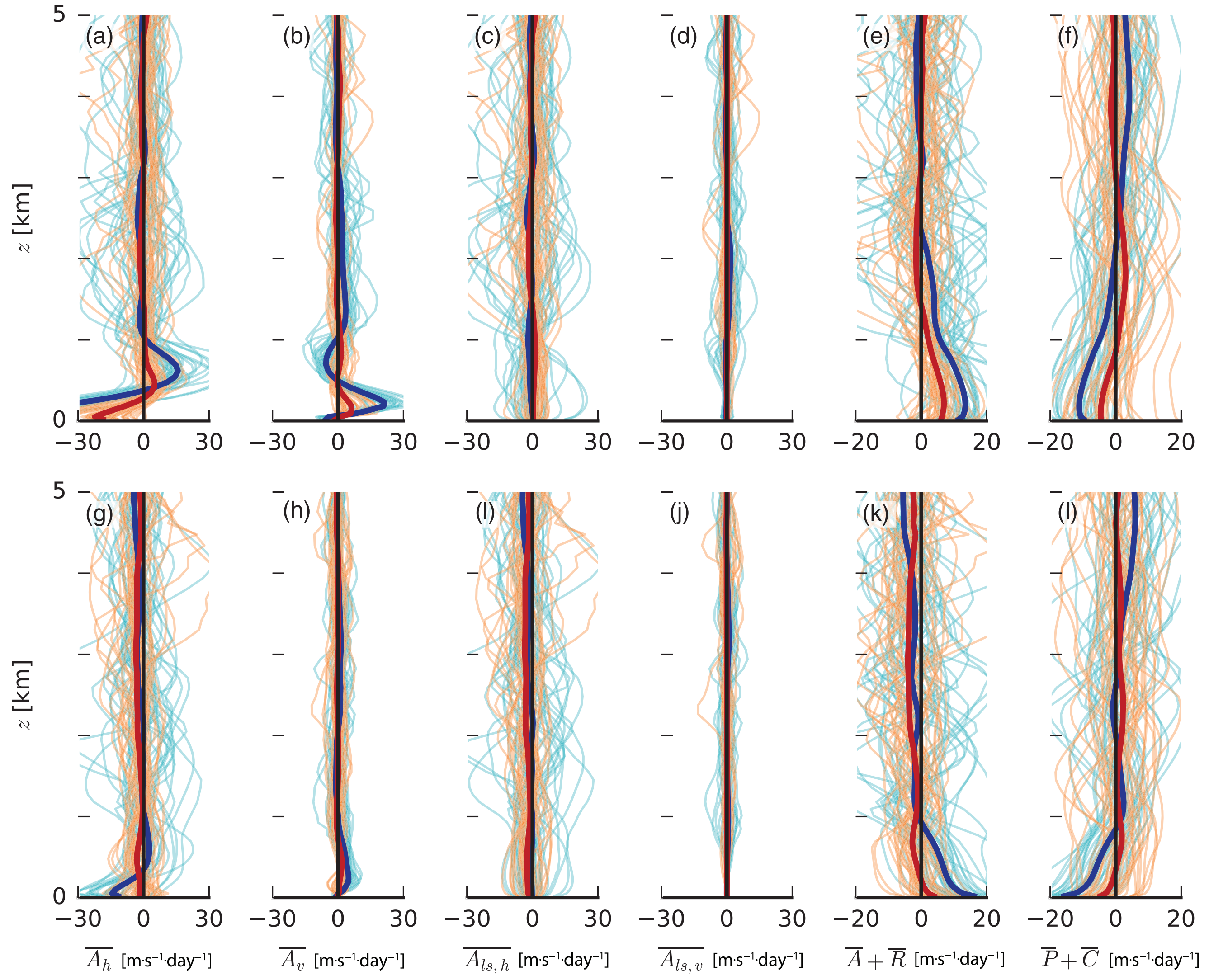

FIGURE 6 Slab-averaged profiles of (a“g) horizontal and (b, h) vertical advection, A_h and A_v, respectively, (c, i) large-scale horizontal and (d, j) large-scale vertical advection, $A_\mathrm{ls,h}$ and $A_\mathrm{ls,v}$, respectively, (e, k) the sum of total resolved advection and residual $A + R$ and (f, l) the sum of pressure-gradient and Coriolis force $P + C$ for (a–f) the zonal wind component and (g–l) the meridional component. The line styles and colours are the same as in Figure 2 [Colour figure can be viewed at wileyonlinelibrary.com]

easterly flow, as seen in Figure 4d. This may be interpreted as CMT removing air from near the surface, where it has gained a westerly wind component due to surface layer turbulent stresses. Similarly, the resolved meridional flux divergence mostly has the same sign as the surface v, indicating an acceleration of the surface wind due to CMT. At cloud base, both the zonal and the meridional flux divergences act to decelerate the flow. In the zonal component and in winter, this continues to be the case up to about 2 km. The grid size of 150 m is an inherent length-scale limit in the discussion of the effects of CMT above, but this is an artificial cut-off. Hence, in the following section, we question how these results change if we increase the length-scale (horizontal resolution) to 300 or 600 m.

3.4 | Sensitivity to horizontal resolution

Our area of interest has three LES domains with different horizontal resolutions of 150, 300 and 600 m (Figure 1). Investigating the resolution dependency of our findings allows us to evaluate the role of unresolved motions versus resolved turbulence or convection. We find that the simulated winds and the total advective plus residual tendencies hardly change with resolution (Figure 8a,d,f,i), which shows the large-scale forcing largely sets the frictional tendencies or perhaps that the small-scale processes cannot meaningfully feed back on the large-scale atmosphere. We wonder if this would have been different if a two-way coupling between the LES and the NWP model had been used.

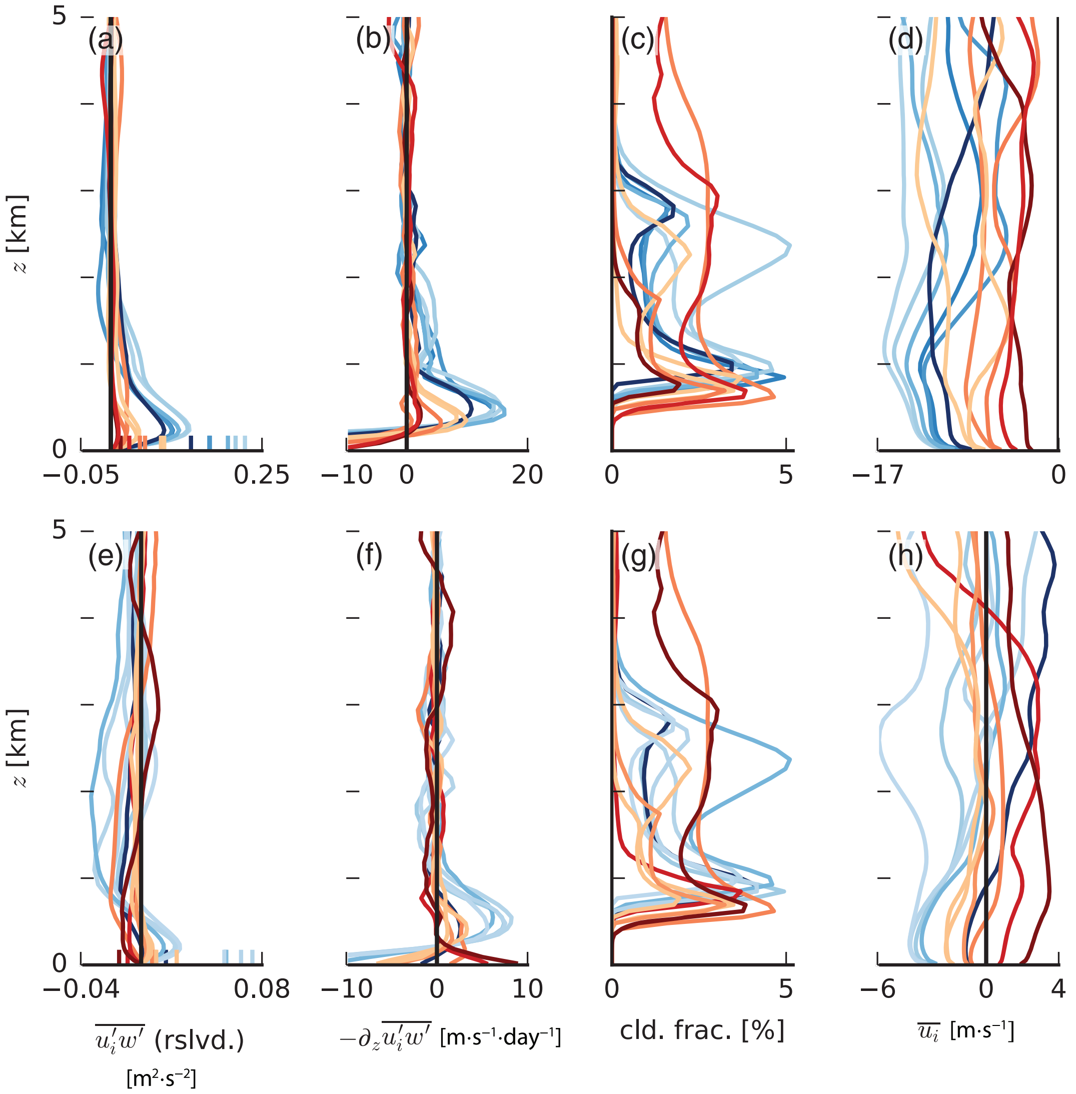

FIGURE 7 Slab-averaged daily profiles of (a, e) the momentum fluxes $\overline{u'w'}$ and $\overline{v'w'}$, (b, f) their negative vertical divergence $-\partial_z\overline{u'w'}$ and $-\partial_z\overline{v'w'}$, (c, g) the cloud fraction and (d, h) the zonal and meridional wind speed. In the top row the lines are coloured by surface zonal wind speed and in the bottom row by the surface meridional wind speed, where blue shades indicate winter days and red shades summer days. The coloured tick marks in (a, e) indicate the surface momentum fluxes [Colour figure can be viewed at wileyonlinelibrary.com]

The tendencies from resolved advection (Figure 8b,g) and from the residual (Figure 8c,h) do change with resolution. The differences are most pronounced when the grid is coarsened from 300 to 600 m, which reduces the resolved zonal momentum flux in the subcloud layer to half its value (Figure 8e), as less turbulence is resolved by the model. Furthermore, the zonal wind tendency due to advection is reduced to zero (or to slightly negative values) in the subcloud layer (Figure 8b), where the residual takes over. Because 600 m is approximately the subcloud-layer depth, this implies that overturning circulations associated with dry convection play a key role at introducing friction below and near cloud base. The deceleration of easterly winds by unresolved turbulence in the lower cloud layer is independent of resolution (Figure 8c,h) and presumably caused by the zonal wind jet above cloud base (Figure 8a) (and the meridional wind jet in the surface layer; Figure 8f), which can introduce significant shear-induced stresses.

3.5 | Momentum transport in moist regions

To highlight the action of moist convection in setting the momentum flux divergence, we may sample the moistest grid points using the upper quartile of the distribution of column-integrated water vapour (*CWV*) and contrast them with the driest quartile, presumably representing cloudy and clear-sky regions, respectively. We calculate

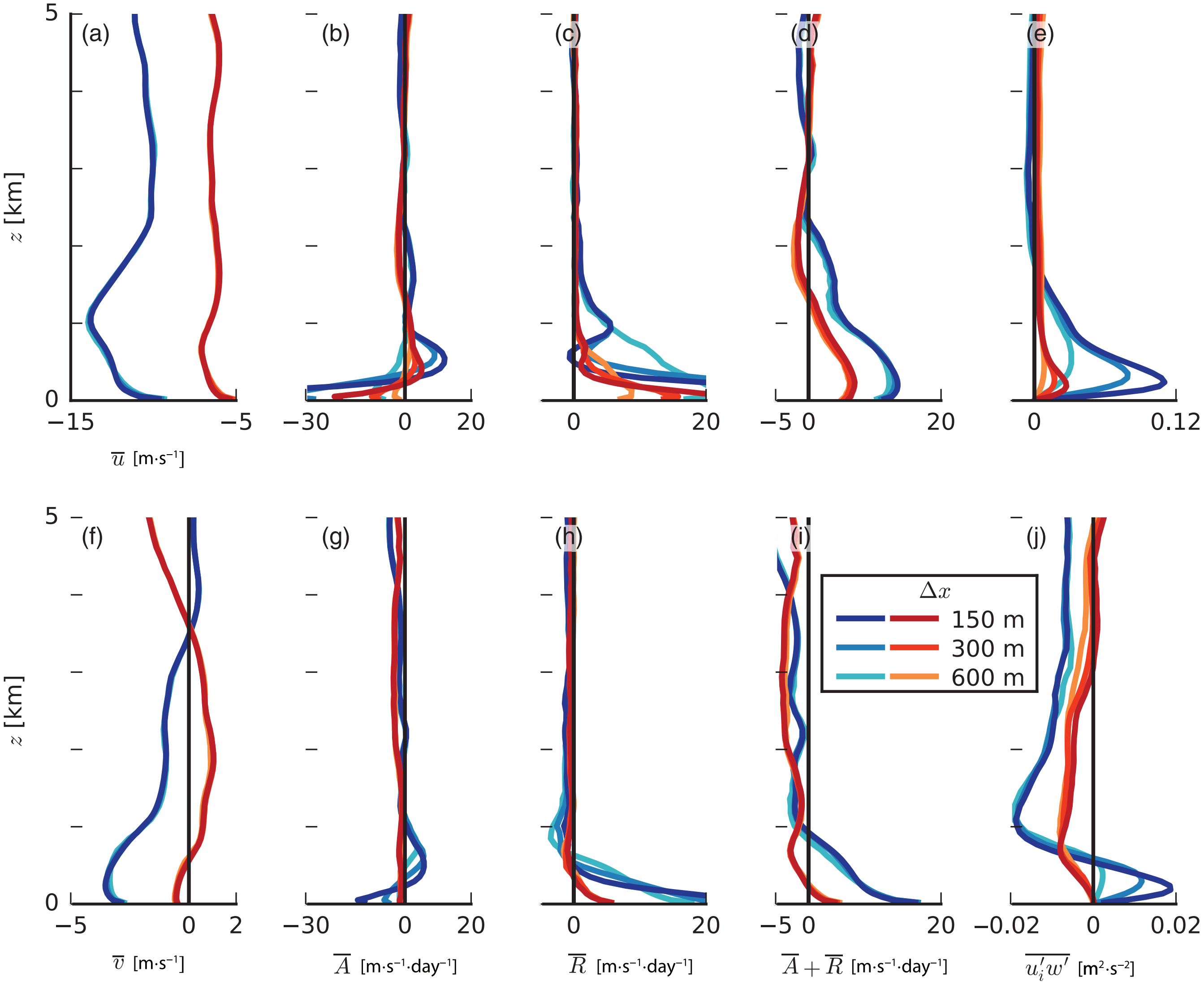

FIGURE 8 Seasonally averaged profiles of (a, f) the wind speed components u and v, (b, g) advection A, (c, h) residual R, (d, i) the sum of resolved advection and residual $A+R$ and (e, j) turbulent momentum flux $\overline{u'w'}$ for different horizontal LES resolutions Δx and for (a–e) the zonal wind component and (f–j) the meridional component. Blue/cyan lines depict winter and red/orange lines summer [Colour figure can be viewed at wileyonlinelibrary.com]

daily averaged momentum flux profiles for the individual quartiles, and average these over winter and summer days (Figure 9a,b for winter and c,d for summer).

First considering winter (Figure 9a,b), we find that the momentum flux profile in the first (Q1, dry) and the second and third quartiles (Q2&Q3) approaches zero at 1 km, whereas the moistest columns (Q4) have a much deeper layer of positive momentum flux (Figure 9a). The differences are not due to different wind profiles, which in fact are very similar for Q1 and Q4 (Figure 9b). Near the cloud-fraction maximum and the zonal-wind jet at about 1 km, there is a thin layer in which the divergence of $u'w'$ in the moistest columns is clearly reduced, indicating a layer of only weak deceleration due to momentum transport, as also seen in Figure 7b. Using the same ICON-LEM data, Dixit *et al.* (2021) show that the momentum flux in positively buoyant updraughts is indeed constant with height or even increases with height in the lower cloud layer. In summer, we find a similar result, whereby moist quartiles with presumably deeper convection lead to the presence of positive momentum flux extending far above the mixed layer, but little divergence (Figure 9c).

4 | COUNTER-GRADIENT MOMENTUM TRANSPORT AND K-DIFFUSION

Coming back to our main question (*What is the role of shallow convection in the momentum budget of the*

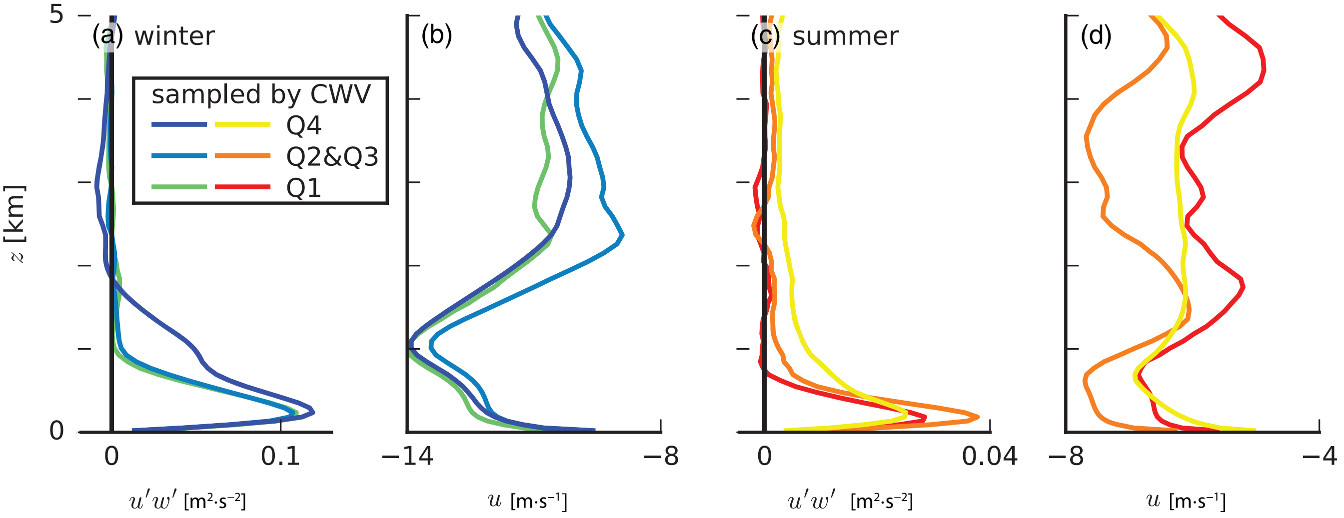

FIGURE 9 Profiles of (a, c) the zonal momentum flux $u'w'$ and (b, d) zonal wind speed averaged over quartiles of the daily column water vapour (*CWV*) distribution for (a, b) all December days and (c, d) all August days [Colour figure can be viewed at wileyonlinelibrary.com]

trades?), we can summarise our findings as follows. The resolved momentum flux associated with cloud-scale and mesoscale circulations (CMT) acts to:

(a) accelerate easterly flow near the surface,
(b) slow down easterly flow in the upper mixed layer and near cloud base, and
(c) slow down easterly flow in the cloud layer.

However, CMT introduces little tendency at the level of the zonal wind jet near 1 km.

Equally important as in the cloud layer appears to be the (dry) convection in the well-mixed subcloud layer. We may use the widely applied K-diffusion approach (also referred to as eddy diffusivity) to evaluate whether the observed momentum fluxes act as so-called down-gradient local turbulent diffusion or as more non-local organised convection. This approach yields a conceptual model for boundary-layer turbulence which has demonstrated skill in explaining surface and boundary-layer winds and is a common boundary-layer parametrization used in global models. It is based on the theoretical assumption that momentum transport is down-gradient and acts to reduce vertical shear in the wind. In the following, we infer how well a K-diffusion model alone would explain the simulated momentum fluxes.

In K-diffusion, the turbulent momentum flux is modelled as the product of the turbulent diffusivity parameter K and the vertical wind gradient:

$$\tau = -\overline{u_i'w'} = K\frac{\partial \overline{u_i}}{\partial z}. \qquad (6)$$

This expression represents the simplest form of the K-diffusion model, in which a non-local term (as discussed in, e.g., Stevens, 2000) is ignored. One may account for non-local turbulence by combining the K-diffusion approach with a mass-flux approach (Soares *et al.*, 2004; Siebesma *et al.*, 2007; Han *et al.*, 2016).

We show that even the simple approach in Equation (6) is able to adequately predict the unresolved momentum fluxes, reconstructing the turbulent momentum flux produced by the K-diffusion approach with input from the LES and comparing it against the actual resolved fluxes. Following Holtslag and Boville (1993), K may be calculated as:

$$K = \kappa w_m z\left(1 - \frac{z}{h}\right)^2, \qquad (7)$$

where $\kappa = 0.4$ is the von Kármán constant, w_m is a turbulent scale velocity and h is the boundary-layer height (here, the cloud-base height). For unstable conditions (such as in the present cases), w_m is proportional to the convective velocity scale w_* (Holtslag and Boville, 1993). Using seasonally averaged surface fluxes (of momentum, heat and moisture) and cloud-base heights h from the simulations, we computed one K profile per season (shown as dotted lines in both Figure 10c,f). These profiles are used to compute momentum fluxes (shown as dotted lines in Figure 10b,e). Also shown in Figure 10 (which zooms in on the lowest 2 km of the atmosphere) are the slab-averaged wind and momentum-flux profiles as calculated from the LES output.

The K-diffusion model seems to produce a reasonable estimation of the (subgrid) turbulent stresses near the surface, where they are close to the surface momentum fluxes output by the LES (indicated by the coloured tick marks in Figure 10b,e). However, above 200 m, coherent structures and larger eddies presumably take over much

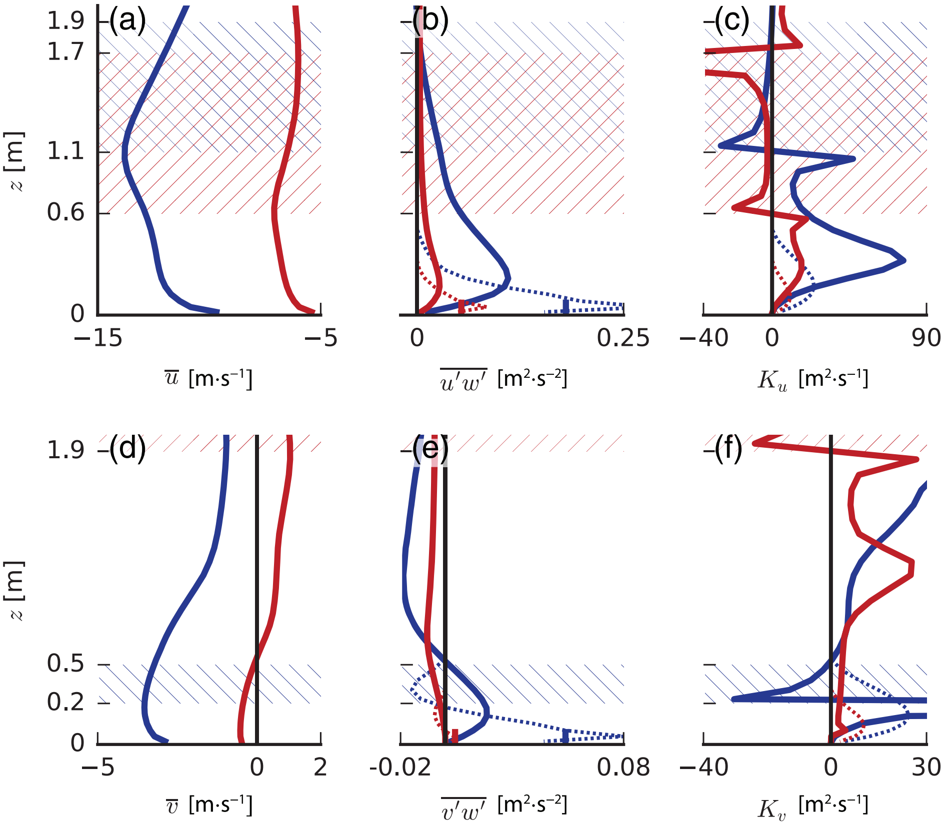

FIGURE 10 Seasonally averaged profiles of (a, d) the wind components u and v, (b, e) the momentum fluxes $u'w'$ and $v'w'$ and (c, f) the turbulent diffusivity parameter K_u and K_v (calculated as the negative ratio of momentum flux and shear (Equation (8)). The hatching indicates altitudes where $K_i < 0$. Blue lines and hatching from top left to bottom right depict winter and red lines and hatching from top right to bottom left summer. The dotted lines in (c, f) indicate the K profile that is computed following Equation (7), and the dotted lines in (b, e) indicate the momentum flux computed from that K (Equation (6)) [Colour figure can be viewed at wileyonlinelibrary.com]

of the transport. It is these fluxes that introduce important tendencies at cloud base. This is also reflected by the fact that the resolved momentum fluxes become more and more resolution-independent with height, which suggests that large-scale overturning is responsible for the friction introduced near cloud base (Figure 8). As mentioned before, combined K-diffusion/mass-flux schemes have been shown to better account for this (Han *et al.*, 2016).

Instead of estimating K based on simulated bulk boundary-layer properties, it can be calculated from our wind and momentum-flux profiles. We rearrange Equation (6) to obtain the turbulent diffusivity parameter K for the zonal and meridional wind separately:

$$K_i = -\frac{\overline{u_i'w'}}{\partial_z \overline{u_i}}. \tag{8}$$

By definition, a positive K_i denotes down-gradient transport, whereby the momentum flux acts to diffuse existing gradients in wind. If $K_i < 0$, the momentum transport is counter-gradient (also referred to as up-gradient), meaning that the momentum flux acts to increase vertical gradients (shear).

The profiles of K_i (shown as solid lines in Figure 10c,f) reveal several layers of counter-gradient momentum transport both in the zonal and the meridional components (indicated by the hatching in Figure 10). From the surface up to the zonal wind jet, turbulent flux of zonal wind is overall down-gradient, but with a notable reduction in K_u between 400 m and 1 km, that is, near cloud base. Above the zonal wind jet, the zonal momentum transport is counter-gradient. The flux vanishes and K_u is zero above 1.7 km.

Although we could not include the subgrid fluxes, which introduce considerable tendencies near the surface and cloud base (Figure 8c,h), we find a similar layered structure in the zonal momentum fluxes as Larson *et al.* (2019) did. While in their BOMEX runs, the counter-gradient layer is some 300 m thick, here it is about twice as thick. In their analysis of the zonal momentum flux budget of the present ICON-LEM simulations, Dixit *et al.* (2021) note that, besides the effective buoyancy production in updraughts, horizontal circulations on scales of several tens of kilometres help increase the presence of (counter-gradient) flux in the cloud layer. However, the production of flux by horizontal circulations is negligible when sampling traditional LES domains on the order of a few $10 \times 10\,\mathrm{km}^2$, which might explain the differences between momentum fluxes in BOMEX and the NARVAL days. During boreal summer, $K_u < 0$ over an even deeper layer, but the gradient in $\overline{u}$ is only very slightly negative and the momentum flux is rather weak across that layer. As described in Larson *et al.* (2019), the counter-gradient flux is a result of updraughts that carry slower momentum ($u' > 0$) across the jet maximum; the momentum flux remains positive until the updraught wind speed has adjusted to the environment at greater heights, even though the local wind gradient has switched sign.

In the meridional component, a jet is present during winter just above the surface layer, along with a roughly 300 m-thick counter-gradient layer above (Figure 10d–f). In summer, this layer is not present because the meridional wind speed is close to zero. Instead, a thick layer of weak counter-gradient flux is present above 1.9 km (reaching up to about 3 km; not shown).

5 | CONCLUSIONS

In this paper, we utilised a unique set of large-eddy-simulation (LES) hindcasts which were run over the North Atlantic (Stevens *et al.*, 2019) to study the role of convective momentum transport (CMT) and small-scale turbulence in the momentum budget of the trades. To our knowledge, the present study is the first one to disentangle small-scale and coherent convective-scale influences on the momentum budget for different seasons from LES. Because the inner LES domains for which we constructed the momentum budget do not have periodic boundary conditions and have been run at different horizontal resolutions, the data allow a unique view on the relative roles of turbulent stresses and resolved motions for a variety of synoptic conditions (in contrast to idealised LES cases).

Asking what the role of shallow convection in the momentum budget of the trades is, our analysis focused on boreal-winter days with steady northeasterly winds and shallow cumulus convection under a strong inversion – typical trade-wind conditions – as well as boreal-summer days with weaker winds from the east, somewhat deeper convection and no inversion. In both seasons the combined pressure-gradient and Coriolis force (setting the geostrophic wind) are of a similar order of magnitude as the combined resolved advection and unresolved turbulent stresses. The influence of 'large-scale' mean horizontal and vertical wind advection appears minor, and we interpret the resolved advection largely as CMT, including thermal and mesoscale circulations which take place in the subcloud and cloud layers. Its structure closely matches that of the vertical divergence of the resolved momentum fluxes.

The combined effect of CMT and unresolved turbulence, which we may label as an ageostrophic or frictional term, is to decelerate the easterly trade winds. Especially in winter, when the wind profile exhibits a strong zonal wind jet near cloud base and larger vertical shear in the easterly wind in the cloud layer, the frictional layer is pronounced and extends up to 2 km. However, CMT has a very different effect depending on the altitude considered; it acts to accelerate near-surface winds, by removing air that has gained a westerly component due to surface friction, to slow down winds in the central and upper mixed layer and finally, to introduce a small amount of 'cumulus friction' in the cloud layer. Notably, CMT introduces little tendency at cloud base where the zonal wind jet resides. By decelerating easterly flow below the jet, it appears to help make the jet more pronounced. In summer, the frictional layer is shallower (only extending up to 1 km) and the friction is overall weaker. The lower depth of the layer reflects the differences in convection: although in summer, there is also deeper convection at times, this hardly contributes to mean cloudiness, and the remaining shallow convection is shallower (Nuijens *et al.*, 2014; Brueck *et al.*, 2015). The weaker frictional force can be attributed to the closer location of the ITCZ in summer, which lessens the pressure gradients, requiring less friction to balance the momentum budget.

On the other hand, unresolved turbulence introduces a frictional force that is largest near the surface, as expected, and reduces in magnitude throughout the mixed layer. However, near cloud base and the zonal wind jet, there is significant unresolved turbulence from scales smaller than 150 m which comprise all of the frictional force there. The momentum flux predicted by a K-diffusion model shows that the flux goes to zero about half way into the mixed-layer, which is where the resolved momentum flux peaks, and where dry convective circulations appear to play an important role. Smaller fluxes which correspond to counter-gradient momentum transport are present above the zonal wind jet (in the cloud layer) and meridional wind jet (above the surface layer), which are a result of slower momentum being carried across these wind speed maxima (Larson *et al.*, 2019).

In conclusion, shallow convection plays an important role in the North Atlantic momentum budget, in particular in decelerating easterly winds below cloud base where momentum fluxes converge. 'Cumulus friction' – a term coined by Schneider and Lindzen (1976) to describe a decelerating effect by (deep) convective momentum transport in the cumulus layer – is not readily present here, as cloud fractions appear too small to introduce large fluxes in the cloud layer. However, there is significant friction near cloud base, which appears associated with smaller-scale turbulent stresses introduced by the zonal wind jet, and from the clouds themselves.

ACKNOWLEDGEMENTS

We thank Matthias Brueck and Daniel Klocke who ran the ICON-LEM simulations for making available the data and for the support with questions regarding the simulation set-up. The data are archived at the German Climate Computing Center (DKRZ) and can be made available upon request. K.C.H. wishes to thank Bjorn Stevens and Cathy Hohenegger for hosting him at the Max Planck Institute for Meteorology in Hamburg, Germany during parts of this project as well as for inspiring discussions. Finally, we thank two anonymous reviewers for their comments which improved this manuscript.

CONFLICT OF INTEREST

The authors declare no conflicting interests.

ORCID

Kevin C. Helfer https://orcid.org/0000-0001-9275-2995
Louise Nuijens https://orcid.org/0000-0003-0989-7443
Vishal V. Dixit https://orcid.org/0000-0002-1468-5253

REFERENCES

Augstein, E., Schmidt, H. and Ostapoff, F. (1974) The vertical structure of the atmospheric planetary boundary layer in undisturbed trade winds over the Atlantic Ocean. *Boundary-Layer Meteorology*, 6, 129–150.

Back, L.E. and Bretherton, C.S. (2009) On the relationship between SST gradients, boundary-layer winds, and convergence over the tropical oceans. *Journal of Climate*, 22, 4182–4196.

Brueck, M., Nuijens, L. and Stevens, B. (2015) On the seasonal and synoptic time-scale variability of the North Atlantic trade wind region and its low-level clouds. *Journal of the Atmospheric Sciences*, 72, 1428–1446.

Brümmer, B., Augstein, E. and Riehl, H. (1974) On the low-level wind structure in the Atlantic trade. *Quarterly Journal of the Royal Meteorological Society*, 100, 109–121.

Carr, M.T. and Bretherton, C.S. (2001) Convective momentum transport over the tropical Pacific: Budget estimates. *Journal of the Atmospheric Sciences*, 58, 1673–1693.

Deser, C. (1993) Diagnosis of the surface momentum balance over the tropical Pacific Ocean. *Journal of Climate*, 6, 64–74.

Dipankar, A., Stevens, B., Heinze, R., Moseley, C., Zängl, G., Giorgetta, M. and Brdar, S. (2015) Large-eddy simulation using the general circulation model ICON. *Journal of Advances in Modeling Earth Systems*, 7, 963–986.

Dixit, V.V., Nuijens, L. and Helfer, K.C. (2021) Counter-gradient momentum transport through subtropical shallow convection in ICON-LEM simulations. *Journal of Advances in Modeling Earth Systems*. https://doi.org/10.1002/essoar.10504427.1. Available at Earth and Space Science Open Archive.

Han, J., Witek, M.L., Teixeira, J., Sun, R., Pan, H.-L., Fletcher, J.K. and Bretherton, C.S. (2016) Implementation in the NCEP GFS of a Hybrid Eddy-Diffusivity Mass-Flux (EDMF) boundary-layer parameterization with dissipative heating and modified stable boundary-layer mixing. *Weather and Forecasting*, 31, 341–352.

Holland, J.Z. and Rasmusson, E.M. (1973) Measurements of the atmospheric mass, energy, and momentum budgets over a 500-kilometer square of tropical ocean. *Monthly Weather Review*, 101, 44–55.

Holtslag, A.A. and Boville, B.A. (1993) Local versus nonlocal boundary-layer diffusion in a global climate model. *Journal of Climate*, 6, 1825–1842.

Klocke, D., Brueck, M., Hohenegger, C. and Stevens, B. (2017) Rediscovery of the doldrums in storm-resolving simulations over the tropical Atlantic. *Nature Geoscience*, 10, 891–896.

Larson, V.E., Domke, S. and Griffin, B.M. (2019) Momentum transport in shallow cumulus clouds and its parameterization by higher-order closure. *Journal of Advances in Modeling Earth Systems*, 11, 3419–3442.

Lin, J.L., Mapes, B.E. and Han, W. (2008) What are the sources of mechanical damping in Matsuno–Gill-type models?. *Journal of Climate*, 21, 165–179.

Malkus, J.S. (1958) On the structure of the trade wind moist layer. *Papers in Physical Oceanography and Meteorology*, 13. https://doi.org/10.1575/1912/5443.

Naumann, A.K. and Kiemle, C. (2020) The vertical structure and spatial variability of lower-tropospheric water vapor and clouds in the trades. *Atmospheric Chemistry and Physics*, 20, 6129–6145.

Neggers, R.A., Neelin, J.D. and Stevens, B. (2007) Impact mechanisms of shallow cumulus convection on tropical climate dynamics. *Journal of Climate*, 20, 2623–2642.

Nuijens, L., Serikov, I., Hirsch, L., Lonitz, K. and Stevens, B. (2014) The distribution and variability of low-level cloud in the North Atlantic trades. *Quarterly Journal of the Royal Meteorological Society*, 140, 2364–2374.

Richter, I., Behera, S.K., Doi, T., Taguchi, B., Masumoto, Y. and Xie, S.-P. (2014) What controls equatorial Atlantic winds in boreal spring?. *Climate Dynamics*, 43, 3091–3104.

Riehl, H., Yeh, T.C., Malkus, J.S. and La Seur, N.E. (1951) The northeast trade of the Pacific Ocean. *Quarterly Journal of the Royal Meteorological Society*, 77, 598–626.

Sato, Y., Shima, S. and Tomita, H. (2018) Numerical convergence of shallow convection cloud field simulations: Comparison between double-moment Eulerian and particle-based Lagrangian microphysics coupled to the same dynamical core. *Journal of Advances in Modeling Earth Systems*, 10, 1495–1512.

Schneider, E.K. and Lindzen, R.S. (1976) A discussion of the parameterization of momentum exchange by cumulus convection. *Journal of Geophysical Research*, 81, 3158–3160.

Siebesma, A.P., Soares, P.M.M. and Teixeira, J. (2007) A combined eddy-diffusivity mass-flux approach for the convective boundary layer. *Journal of the Atmospheric Sciences*, 64, 1230–1248.

Soares, P.M.M., Miranda, P., Siebesma, A.P. and Teixeira, J. (2004) An eddy-diffusivity/mass-flux parametrization for dry and shallow cumulus convection. *Quarterly Journal of the Royal Meteorological Society*, 130, 3365–3383.

Stevens, B. (2000) Quasi-steady analysis of a PBL model with an eddy-diffusivity profile and nonlocal fluxes. *Monthly Weather Review*, 128, 824–836.

Stevens, B., Duan, J., McWilliams, J.C., Münnich, M. and Neelin, J.D. (2002) Entrainment, Rayleigh friction, and boundary-layer winds over the tropical Pacific. *Journal of Climate*, 15, 30–44.

Stevens, B., Ament, F., Bony, S., Crewell, S., Ewald, F., Gross, S., Hansen, A., Hirsch, L., Jacob, M., Kölling, T., Konow, H., Mayer, B., Wendisch, M., Wirth, M., Wolf, K., Bakan, S., Bauer-Pfundstein, M., Brueck, M., Delanoë, J., Ehrlich, A., Farrell, D., Forde, M., Gödde, F., Grob, H., Hagen, M., Jäkel, E., Jansen, F., Klepp, C., Klingebiel, M., Mech, M., Peters, G., Rapp, M., Wing, A.A. and Zinner, T. (2019) A high-altitude long-range aircraft configured as a cloud observatory: the NARVAL expeditions. *Bulletin of the American Meteorological Society*, 100, 1061–1077.

Stevens, B., Bony, S., Farrell, D., Ament, F., Blyth, A., Fairall, C., Karstensen, J., Quinn, P.K., Speich, S., Acquistapace, C., Aemisegger, F., Albright, A.L., Bellenger, H., Bodenschatz, E., Caesar, K.-A., Chewitt-Lucas, R., de Boer, G., Delanoë, J., Denby, L., Ewald, F., Fildier, B., Forde, M., George, G., Gross, S., Hagen, M., Hausold, A., Heywood, K.J., Hirsch, L., Jacob, M., Jansen, F., Kinne, S., Klocke, D., Kölling, T., Konow, H., Lothon, M., Mohr, W., Naumann, A.K., Nuijens, L., Olivier, L., Pincus, R., Pöhlker, M., Reverdin, G., Roberts, G., Schnitt, S., Schulz, H., Siebesma, A.P., Stephan, C.C., Sullivan, P., Touzé-Peiffer, L., Vial, J., Vogel, R., Zuidema, P., Alexander, N., Alves, L., Arixi, S., Asmath, H., Bagheri, G., Baier, K., Bailey, A., Baranowski, D., Baron, A., Barrau, S., Barrett, P.A., Batier, F., Behrendt, A., Bendinger, A., Beucher, F., Bigorre, S., Blades, E., Blossey, P., Bock, O., Böing, S., Bosser, P., Bourras, D., Bouruet-Aubertot, P., Bower, K., Branellec, P., Branger, H., Brennek, M., Brewer, A., Brilouet, P.-E., Brügmann, B., Buehler, S.A., Burke, E., Burton, R., Calmer, R., Canonici, J.-C., Carton, X., Cato Jr. G., Charles, J.A., Chazette, P., Chen, Y., Chilinski, M.T., Choularton, T., Chuang, P., Clarke, S., Coe, H., Cornet, C., Coutris, P., Couvreux, F., Crewell, S., Cronin, T., Cui, Z., Cuypers, Y., Daley, A., Damerell, G.M., Dauhut, T., Deneke, H., Desbios, J.-P., Dörner, S., Donner, S., Douet, V., Drushka, K., Dütsch, M., Ehrlich, A., Emanuel, K., Emmanouilidis, A., Etienne, J.-C., Etienne-Leblanc, S., Faure, G., Feingold, G., Ferrero, L., Fix, A., Flamant, C., Flatau, P.J., Foltz, G.R., Forster, L., Furtuna, I., Gadian, A., Galewsky, J., Gallagher, M., Gallimore, P., Gaston, C., Gentemann, C., Geyskens, N., Giez, A., Gollop, J., Gouirand, I., Gourbeyre, C., de Graaf, D., de Groot, G.E., Grosz, R., Güttler, J., Gutleben, M., Hall, K., Harris, G., Helfer, K.C., Henze, D., Herbert, C., Holanda, B., Ibanez-Landeta, A., Intrieri, J., Iyer, S., Julien, F., Kalesse, H., Kazil, J., Kellman, A., Kidane, A.T., Kirchner, U., Klingebiel, M., Körner, M., Kremper, L.A., Kretzschmar, J., Krüger, O., Kumala, W., Kurz, A., L'Hégaret, P., Labaste, M., Lachlan-Cope, T., Laing, A., Landschützer, P., Lang, T., Lange, D., Lange, I., Laplace, C., Lavik, G., Laxenaire, R., Le Bihan, C., Leandro, M., Lefevre, N., Lena, M., Lenschow, D., Li, Q., Lloyd, G., Los, S., Losi, N., Lovell, O., Luneau, C., Makuch, P., Malinowski, S., Manta, G., Marinou, E., Marsden, N., Masson, S., Maury, N., Mayer, B., Mayers-Als, M., Mazel, C., McGeary, W., McWilliams, J.C., Mech, M., Mehlmann, M., Meroni, A.N., Mieslinger, T., Minikin, A., Minnett, P., Möller, G., Morfa Avalos, Y., Muller, C., Musat, I., Napoli, A., Neuberger, A., Noisel, C., Noone, D., Nordsiek, F., Nowak, J.L., Oswald, L., Parker, D.J., Peck, C., Person, R., Philippi, M., Plueddemann, A., Pöhlker, C., Pörtge, V., Pöschl, U., Pologne, L., Posyniak, M., Prange, M., Quiñones Meléndez, E., Radtke, J., Ramage, K., Reimann, J., Renault, L., Reus, K., Reyes, A., Ribbe, J., Ringel, M., Ritschel, M., Rocha, C.B., Rochetin, N., Röttenbacher, J., Rollo, C., Royer, H., Sadoulet, P., Saffin, L., Sandiford, S., Sandu, I., Schäfer, M., Schemann, V., Schirmacher, I., Schlenczek, O., Schmidt, J., Schröder, M., Schwarzenboeck, A., Sealy, A., Senff, C.J., Serikov, I., Shohan, S., Siddle, E., Smirnov, A., Späth, F., Spooner, B., Stolla, M.K., Szkółka, W., de Szoeke, S.P., Tarot, S., Tetoni, E., Thompson, E., Thomson, J., Tomassini, L., Totems, J., Ubele, A.A., Villiger, L., von Arx, J., Wagner, T., Walther, A., Webber, B., Wendisch, M., Whitehall, S., Wiltshire, A., Wing, A.A., Wirth, M., Wiskandt, J., Wolf, K., Worbes, L., Wright, E., Wulfmeyer, V., Young, S., Zhang, C., Zhang, D., Ziemen, F., Zinner, T. and Zöger, M. (2021) EUREC^{4}A. *Earth System Science Data Discussions*. in review. https://doi.org/10.5194/essd-2021-18

Stull, R.B. (1988) *An Introduction to Boundary-Layer Meteorology*. Dordrecht: Kluwer Academic Publishers.

Tiedtke, M., Heckley, W.A. and Slingo, J.M. (1988) Tropical forecasting at ECMWF: the influence of physical parametrization on the mean structure of forecasts and analyses. *Quarterly Journal of the Royal Meteorological Society*, 114, 639–664.

Vial, J., Vogel, R., Bony, S., Stevens, B., Winker, D.M., Cai, X., Hohenegger, C., Naumann, A.K. and Brogniez, H. (2019) A new look at the daily cycle of trade wind cumuli. *Journal of Advances in Modeling Earth Systems*, 11, 3148–3166.

Vogel, R., Bony, S. and Stevens, B. (2020) Estimating the shallow convective mass flux from the subcloud-layer mass budget. *Journal of the Atmospheric Sciences*, 77, 1559–1574.

Zängl, G., Reinert, D., Rípodas, P. and Baldauf, M. (2015) The ICON (ICOsahedral Non-hydrostatic) modelling framework of DWD and MPI-M: Description of the non-hydrostatic dynamical core. *Quarterly Journal of the Royal Meteorological Society*, 141, 563–579.

How to cite this article: Helfer KC, Nuijens L, Dixit VV. The role of shallow convection in the momentum budget of the trades from large-eddy-simulation hindcasts. *QJR Meteorol. Soc.* 2021;147:2490–2505. https://doi.org/10.1002/qj.4035